BILINGUAL PUBLISHING GROUP

Journal of Atmospheric Science Research

https://journals.bilpubgroup.com/index.php/jasr

ARTICLE

Formation and Transport of a Saharan Dust Plume in Early Summer

***Habib Senghor*[1*], *Abdou L. Dieng*[2], *Moussa Gueye*[3], *Cheikh A. Diop*[1], *Mariane D. Kane*[1], *Amadou T. Gaye*[2]**

[1] *Agence Nationale de l'Aviation Civile et de la Météorologie, Dakar, 8184, Sénégal*

[2] *Laboratoire de Physique de l'Atmosphère et de l'Océan Siméon-Fongang (LPAO-SF), Université Cheikh Anta Diop, Dakar, 10700, Sénégal*

[3] *Département de Mathématiques et Informatiques, Université du Sine Saloum Elhadj Ibrahima Niass, Kaolack BP 55, Sénégal*

ABSTRACT

This research studies the capability of the Weather Research and Forecasting model coupled with the Chemistry/Aerosol module (WRF-Chem) with and without parametrization to reproduce a dust storm, which was held on 27th June 2018 over Sahara region. The authors use satellite observations and ground-based measurements to evaluate the WRF-Chem simulations. The sensitivities of WRF-Chem Model are tested on the replication of haboob features with a tuned GOCART aerosol module. Comparisons of simulations with satellite and ground-based observations show that WRF-Chem is able to reproduce the Aerosol Optical Depth (AOD) distribution and associated changes of haboob in the meteorological fields with temperature drops of about 9 °C and wind gust 20 $m \cdot s^{-1}$. The WRF-Chem Convection-permitting model (CPM) shows strong 10-meter winds induced a large dust emission along the leading edge of a convective cold pool (LECCP). The CPM indicates heavy dust transported over the West African coast (16°W-10°W; 6°N-21°N) which has a potential for long-distance travel on 27th June between 1100 UTC and 1500 UTC. The daily precipitation is improved in the CPM with a spatial distribution similar to the GPM-IMERG precipitation and maximum rainfall located at the right place. As well as raising a large amount of dust, the haboob caused considerable damage along its route.

Keywords: Dust storm; WRF-Chem; Convection-permitting; Parameterization; MCS

*CORRESPONDING AUTHOR:

Habib Senghor, Agence Nationale de l'Aviation Civile et de la Météorologie, Dakar, 8184, Sénégal; Email: habib.senghor@anacim.sn

ARTICLE INFO

Received: 12 January 2023 | Revised: 06 April 2023 | Accepted: 10 April 2023 | Published Online: 14 April 2023

DOI: https://doi.org/10.30564/jasr.v6i2.5407

CITATION

Senghor, H., Dieng, A.L., Gueye, M., et al., 2023. Formation and Transport of a Saharan Dust Plume in Early Summer. Journal of Atmospheric Science Research. 6(2): 58-74. DOI: https://doi.org/10.30564/jasr.v6i2.5407

1. Introduction

As a major contributor to global dust emissions, the North African region plays an important role in the Earth's climate by scattering and absorbing incoming solar radiation and changing the physical properties of clouds [1]. Dust particles can be used in cloud formation as giant cloud condensation nuclei which can affect the microphysics development of clouds [2]. The effect of mineral dust on the cloud properties is to inhibit precipitation [3]. However, the role of Saharan dust on rainfall remains poorly understood [4] since research works showed, on contrary, that dust could enhance the precipitation in numerical weather prediction (NWP) models [5]. Kocha et al. [6] highlighted the necessity to couple the NWP forecasting models with an aerosol module [6]. The utilization of a dust scheme in NWM could contribute to improving the cloud cover in West Africa [7]. In this region, the mesoscale convective systems contribute the most to the precipitation during the monsoon season [8]. The total precipitation is generated particularly up to 90% by the convective storms in West Africa [9]. The convective storms generate downdrafts and cold pools over dry dusty surfaces producing large dust storms [10]. The haboobs are dust storms produced by the spreading of evaporatively cooled air from thunderstorms over the dusty area [10]. Several thunderstorms produce mesoscale convective systems when they merge to create a continuous area of convective instability that persists at least for several hours and produces a continuous precipitation area [11].

Finney et al. [12] have highlighted the limitation of the Parameterized models (PM) due to their approximations in the representation of the convection. Using two simulations with 12 km horizontal grid spacing, one running with Parameterized and the other with explicit convection, Birch et al. [13] showed a significant bias of the diurnal water cycle. The uncertainties of the diurnal water cycle have induced an increase in the northward advection of the moisture into Sahel [13]. Marsham et al. [14] showed that simulations of the West African monsoon explicitly resolve moist convection with simulations which parameterize convection with the UK Met Office Unified Model with 12 km grid spacing. By using the dust uplift potential (DUP), which represents the dependency of dust uplift on wind speed for an idealized land surface, Marsham et al. [15] showed that haboobs are absent in models with parametrized convection. These failures have been linked to systematic errors [16]. On the other hand, several studies showed that CPM can be helpful for improving rainfall [13,17,18] by reducing the biases of the diurnal cycle of simulated precipitation, extreme precipitation, cloud cover, and radiation [18]. The explicit convection improves the intensity of storms and the West Africa monsoon [19,20]. Nevertheless, the meteorological features are not improved in whole aspects of the CPM model [18,21].

This study aims to examine the ability of WRF-chem to reproduce a dust storm and the mesoscale characteristics associated with the event, from 26 to 27 June 2018 over Western Africa, by using parametrized and explicit convection. The impact of dust on solar radiation, 2-meter temperatures and changes including precipitation is also studied using an additional simulation with no dust activation (NODUST).

The paper is organized as follows. Datasets, model experiments and methodology are described in Section 2. The satellite observations and ground measurements are used to describe the synoptic state of the event in Section 3.1. The evaluation of simulated dust AOD is presented in Section 3.2. The properties of the storm in the model simulations are analyzed in Sections 3.3 and 3.4. The impact of the dust on the radiative budget is investigated in Section 3.5. Finally, the conclusion is given in Section 4.

2. Data and method

2.1 Observations

The moderate resolution imaging spectroradiometer (MODIS) is a passive imaging radiometer that measures reflected radiation and emitted thermal

radiation in 36 bands. The dataset is provided with 10 km as a horizontal resolution for a better comparison with simulated AOD [22]. Cold pools can be discriminated in the dust channels with dark color and mineral dust with pink color [23]. The identification of dust depends strongly on the column water vapor, the lower tropospheric lapse rate, and dust altitude. Dust is particularly masked when the water vapor exceeds 25 mm [23].

The moderate resolution imaging spectroradiometer (MODIS) is a passive imaging radiometer and measures reflected radiation and emitted thermal radiation in 36 bands. Dataset are provided with 10 km as horizontal resolution for a better comparison with simulated AOD [24]. We use MODIS/Aqua level-3 atmosphere daily global product which overpass above Western Africa in the afternoon.

The Infrared Atmospheric Sounding Interferometer (IASI) algorithm, which enables to retrieval of optical and microphysical properties of aerosol types [25], is used to retrieve dust AOD during the event.

The Visible Infrared Imaging Radiometer Suite (VIIRS) deep blue Aerosol Optical Thickness (AOT) layer is taken from the National Aeronautics and Space Administration (NASA)/National Oceanic and Atmospheric Administration (NOAA) Suomi National Polar-Orbiting Partnership (Suomi NPP) satellite for the daytime overpass. The imagery resolution is 2 km at nadir, and the temporal resolution is daily [26,27].

The Global Precipitation Measurement (GPM) was launched on 27 February 2014 by NASA in association with the Japan Aerospace Exploration Agency (JAXA) to provide a higher spatiotemporal resolution product for global precipitation between 60°S and 60°N [28]. We use 24 h accumulated rainfall from Integrated Multi-satellite Retrievals for Global Precipitation Measurement (IMERG) version V06 with a 0.1° × 0.1° spatial grid.

The fifth generation of reanalysis from the European Center for Medium-Range Weather Forecasts (ECMWF) ERA5 is used to investigate the synoptic situation preceding the initiation of the MCS. The ERA5 dataset is provided at a 1-hourly time step and is gridded to a regular latitude-longitude of 31 km horizontal resolution and 139 pressure levels [29].

2.2 Model description and experimental setup

We use the WRF model version 3.7.1 coupled with chemistry which enables the simulation of aerosols and trace gases with meteorological fields [30]. Both models are run from 15 to 29 June with one-day spin-up. Daily mean AOD from 16 at 00:00 and 29 June at 23:00 in 2018 are computed boundary conditions provided by NOAA/National Centers for Environmental Prediction Final Analysis (NCEP-FNL) with a horizontal grid spacing of 0.5° × 0.5° and interpolated by WRF preprocessing system and update every 6 hours. The simulation domain is centered in North Mali (1°W, 19°N) and contains 390 × 250 horizontal grid points with 9 km resolution and 51 vertical levels extending up to 50 hPa. The configuration of the model uses the Goddard Global Ozone Chemistry Aerosol Radiation and Transport (GOCART) module [31] to simulate mineral dust concentration PM10 and AOD. The Yonsei University (YSU) planetary boundary layer scheme [32], the Noah land-surface model [33], the revised Mesoscale Model (MM5) scheme [34], the Rapid Radiative Transfer Model for Global models (RRTMG) for shortwave [35] and RRTM for longwave radiation [36], the Grell cumulus parametrization [37] and WRF Single-Moment 5-class (WSM5) microphysics schemes [38] are used by the configuration (**Table 1**). The aerosol feedback which provides a reduction in downward solar radiation from aerosol scattering is taken into account [39]. The Parameterized (PM) and the CPM models used the same configuration except that cumulus (CU) parametrization is not activated in the CPM model. A control simulation is also run to evaluate the impact of dust in the 2 m temperature.

2.3 Model tuning

The sensitivity tests which consist to adjust the coefficient of dust emission flux are performed with

the GOCART aerosol module in both PM and CPM models. In this study, the GOCART dust scheme parametrization is tuned by calibrating dust emission to match observed AOD from AERONET (not shown) and satellites retrieved AOD averaged in the entire domain (**Figure 1**). For this purpose, the coefficient C in Equation (1), which was originally estimated to be 0.8 $mg \cdot s^2 \cdot m^{-5}$ [31] in version 3.7.1, is adjusted to achieve the most agreement with observed AOD [40,41]. The dust emission mass flux, *Fp* ($\mu g \cdot m^{-2} \cdot s^{-1}$), for a specific aerosol size group *p* is defined as followed:

$$F_p = \begin{cases} CSS_p (U^2_{10m} - U_t) & if\ U_{10m} > Ut, \\ 0 & otherwise \end{cases} \quad (1)$$

where, *C* is a dimensional constant coefficient that controls the magnitude of dust emission flux; *S* is the source function that characterizes the spatial distribution of dust emission; *U10m* is the horizontal wind speed at 10 m; *Ut* is the threshold velocity of wind erosion, which depends on particle size and wetness; and *Sp* is a fraction of mass emitted into size group *p*.

Table 1. Physical and chemical schemes used in the WRF-Chem simulations.

Simulation settings	**Values**
Domain size	390 × 250 cells
Horizontal resolution	9 km
Vertical resolution	51 levels up to 50 hPa
Time step for physics	60 s
Time step for chemistry	60 s
Physics options	**Used schemes**
Microphysics	WSM5
Longwave radiation	RRTM
Shortwave radiation	RRTMG
Surface layer	Revised MM5
Surface land	Noah and land surface model
Planetary boundary layer	YSU
Cumulus parametrization	Grell-3
Chemistry options	**Used schemes**
Chemistry	GOCART simple aerosol scheme, no ozone chemistry

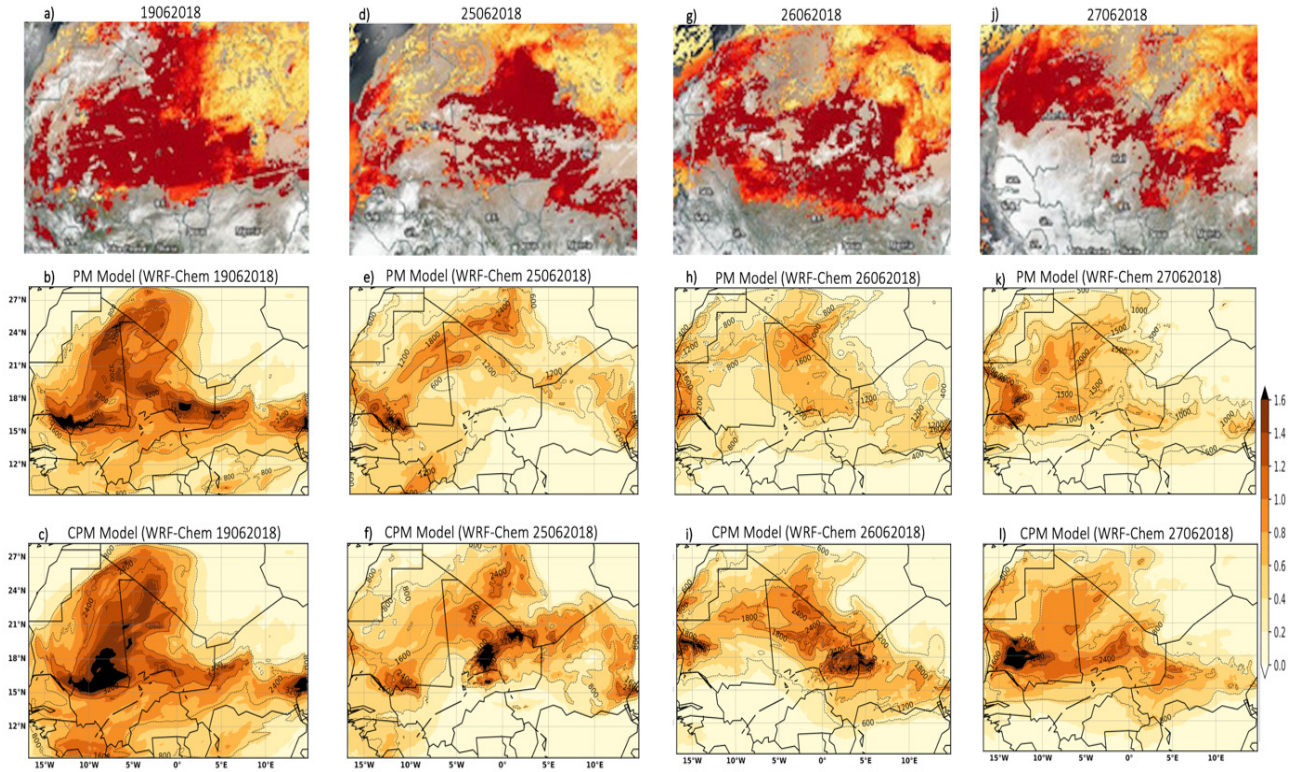

Figure 1. Daily mean AOD observed by NASA Worldview (top panel), daily average simulated AOD are shown by the color shading and PM10 concentration in $\mu g \cdot m^{-3}$ are represented by the black contour respectively by WRF-Chem Parameterized (PM) model (middle panel), and WRF-Chem Convection-permitting model (CPM) (bottom panel) on (a-b-c) 19 June 2018, on (d-e-f) 25 June, (g-h-i) on 26 June, and (j-k-l) on 27 June.

3. Results and discussion

3.1 Observations of synoptic situation

Figure 2 and **Figure 3** show the evolution of the synoptic-scale meteorology which has provided the formation of the MCS. The synoptic situation for this case study includes the mean sea-level pressure, the position of the ITD defined by the 14 °C isotherm of the 2 m dewpoint temperature, and the relative humidity for **Figure 2**. Complementary information for the synoptic situation is given in **Figure 3** and is based on the 200 hPa geopotential, 925 wind speed, and 925 hPa streamlines. The description of the synoptic situation covers twelve days from 16 to 27 June and uses the daily mean ERA5 Reanalysis. Ten (10) days before the event (16 June), a core of low pressure of 1008 hPa (**Figure 2a**) is located over North Mali and four (04) days after central Mali with a lower pressure of 1006 hPa (**Figure 2b**). This southward transport of the core of low pressure brings dry air masses from the northern Sahara to Sahel region up to 12°N. On 24 June, the monsoon trough is located further north involving a strong shift of the Intertropical Discontinuity (ITD) [22] to the south of Algeria (**Figure 2c**). On 23 June (**Figure 2d**), the ITD is almost zonal and located further north and the low-pressure core is located over the Western Africa coastal region. On the day of the event, the ITD is still further north and strong contrast is observed in the relative humidity between Sahara and Gulf of Guinea. From 24 to 26 June, there is an anticyclone characterizing by a high geopotential at the upper level over boundaries between Algeria, Mali and Mauritania and generating heavy dust emission over the same area as shown in **Figure 1**. This produces

a strong southward dust transport with high wind speed at 925 hPa and the southward shift of the ITD from south Algeria to northwest Niger (**Figure 2e**).

The thermodynamic properties of the cold pool are studied at the time of detection of the cold pool over Kayes and Matam (**Figures 4e** and **4f**) [42]. The haboob was detected at 0900 UTC over Kayes in western Mali (**Figure 4c**) and at 1000 UTC over Matam (**Figure 4d**) on 27 June. Sudden changes are associated with the location of the MCS over Eastern and Western Senegal both with a greater decrease of the temperature of about 9 °C [42]. The maximum wind speeds are obtained about 1-hour before the arrival of the MCS at the stations as already observed during the Fennec field campaign by Allen et al. [43].

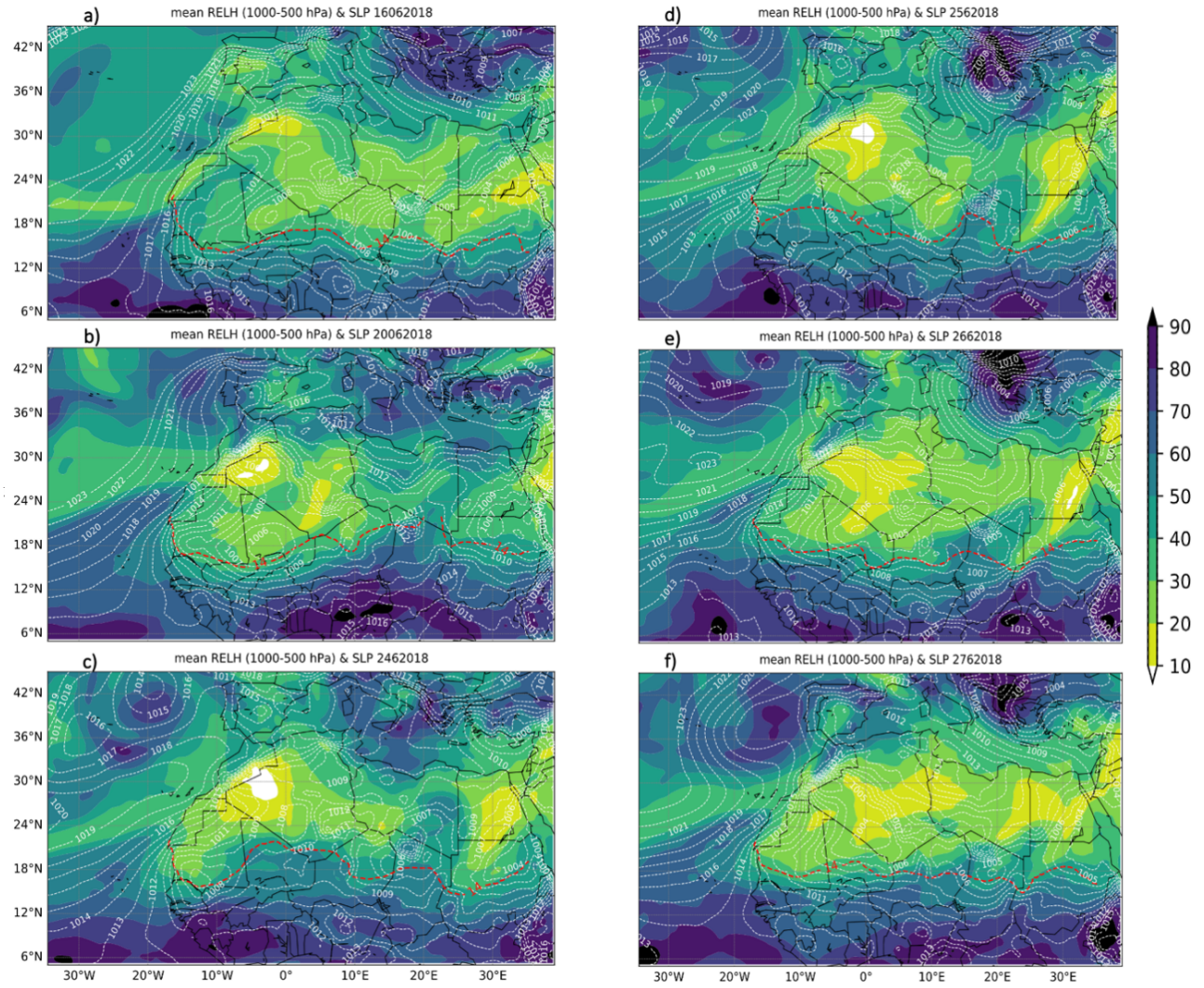

Figure 2. Synoptic state before and during the establishment of the haboob in the western Africa region on (a) 16 June 2018, (b) 20 June, (c) 24 June, (d) 25 June, (e) 26 June, and (f) 27 June. The ITD from ERA5 Re-Analysis is defined by the 14 °C isotherm of 2m dewpoint temperature (dashed red line), mean sea-level pressure in hPa (dashed with line) and relative humidity (color shading).

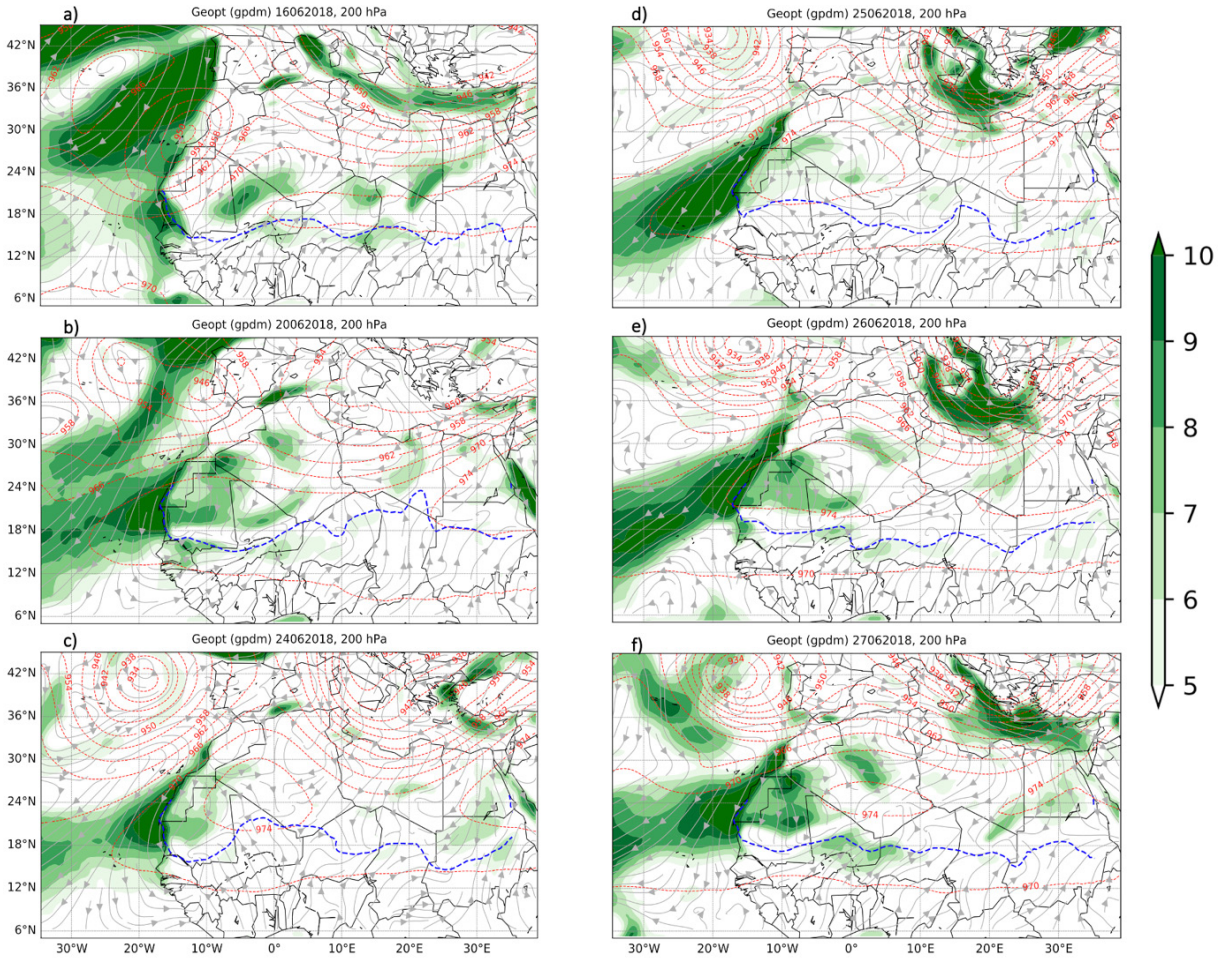

Figure 3. Synoptic state before and during the establishment of the haboob over the western Africa region on (a) 16 June 2018, (b) 20 June, (c) 24 June, (d) 25 June, (e) 26 June, and (f) 27 June. The ITD from ERA5 Re-Analysis is shown over land (dashed blue line), 200 hPa geopotential (dashed red line), 925 hPa wind speed (green shading) overlain with 925 hPa streamlines (grey).

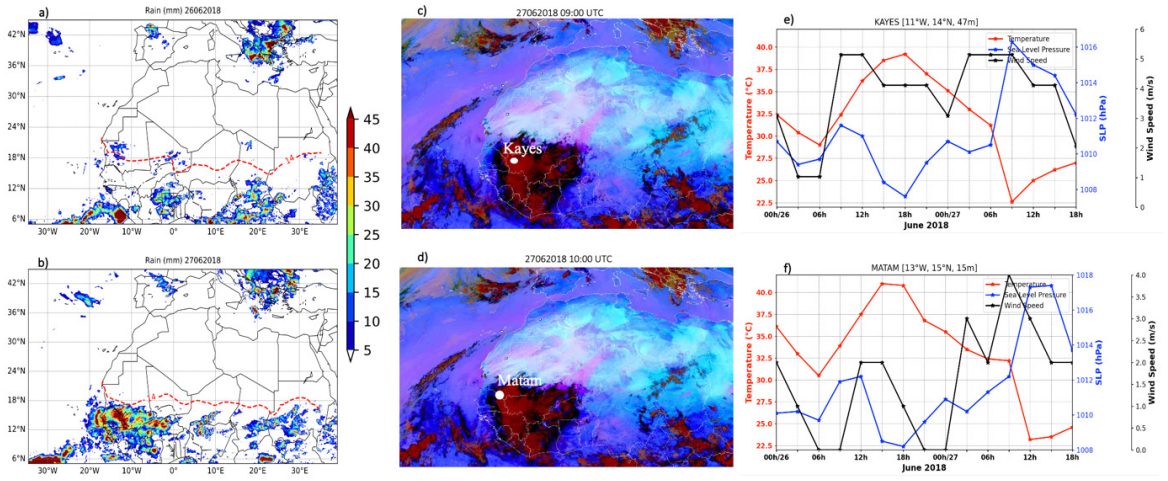

Figure 4. ITD from ERA5 (dashed red line), estimated 24 h accumulated rainfall from IMERG on (a) 26 June 2018, and (b) 27 June 2018. Spinning Enhanced Visual and Infrared Imager (SEVIRI) red, green, blue (RGB) dust image (c) at 0900 UTC 27 June 2018, and (d) at 1000 UTC 27 June 2018. Dust is represented by magenta, deep clouds by red, midlevel clouds by orange, cirrus clouds by black, and surface by blue, and white dots show the location of the synoptic station of Kayes (Mali) and Matam (Senegal). The synoptic measurement over Kayes and Matam are respectively shown in (e) and (f). The near-surface temperature is shown by the red line, the wind speed by the black line, and the sea-level pressure by the blue line.

3.2 Assessment of dust

To assess the aerosol integrated-column, we compare AOD from both simulations PM and CPM with the daily retrieved AOD from IASI and MODIS sensors over West Africa (17°W-15°E; 9°N-30°N) between 16 June and 29 June 2018 (**Figure 5a** and **Figure 1**). In General, the simulations conducted by a tuning factor of 1 $mg \cdot s^2 \cdot m^{-5}$ show a good replication of the magnitude and temporal evolution of observed AOD. Between 16 and 21 June, the diurnal variability of observed AOD is reproduced by simulations with a best agreement in the CPM (**Figure 5a** and **Figure 1**). Both simulations are in accordance with observations by capturing the maximum retrieved AOD between 17 and 20 June and minimum AOD between 22 and 29 June (**Figure 5a**). Both models did not match the maximum value of retrieved AOD by satellites on 20 June. The increase tendency of AOD on 25 June is also missed in simulations. **Figure 1** more details in the daily aerosol horizontal distribution of simulated and observed AOD which retrieved from Suomi NPP/VIIRS Deep Blue. The horizontal distribution of AOD showed that both models are able to reproduce the spatial distribution with a better accordance in the CPM. The shape of the dust plume is well replicated in the simulations with a maximum the PM10 concentration of 4000 $\mu g \cdot m^{-3}$ located over the maximum AOD values. On 19 June, the dust emissions were apparent strongly activated with a considerable contribution of Bodélé (Chad) dust source [44] and the Saharan dust source [45] located particularly over southern Algeria, and northern Mali and Mauritania. The magnitude of dust emission as shown by the observations and simulations decreases after 19 June, however the major dust contribution from sources cited above is maintained. On 27 June, when the dust storm occurs, the maximum PM10 isotherm of 2000 and 2400 $\mu g \cdot m^{-3}$ respectively in PM and CPM were located over southern Mauritania.

Figure 6 shows that emitted dust is strongly led by the 10-meter winds which exceed largely the wind threshold of 5.2 $m \cdot s^{-1}$ for desert dust emission [46]. The Outgoing Longwave Radiation (OLR) shows the evolution of the MCS identified by the minimum values less than 240 $W \cdot m^{-2}$ [47]. The MCS is clearly faster and finer in the CPM than in the PM (**Figure 6**). The MCS reaches the eastern boundaries of Senegal at 0000 UTC (**Figure 6a**) and 0300 UTC (**Figure 6d**) respectively in the PM and CPM models.

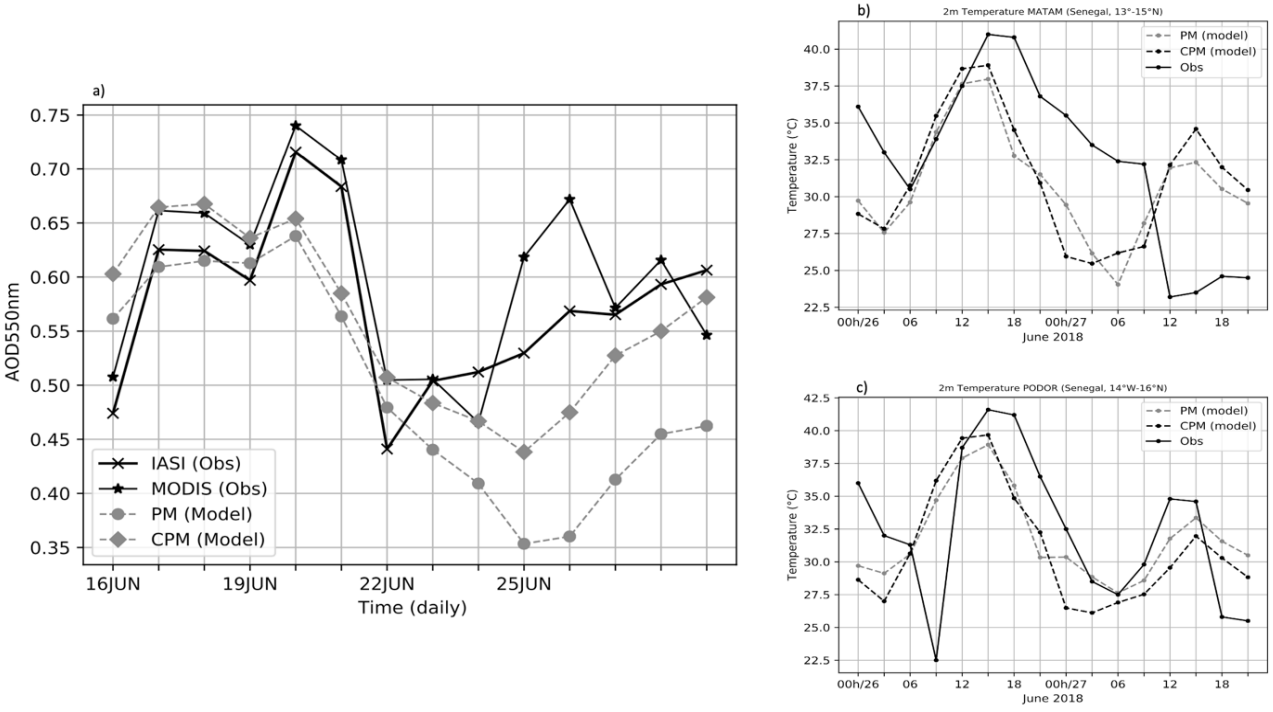

Figure 5. (a) Time series of AOD area averaged over Western Africa (17°W-15°E; 9°N-30°N) observed by MODIS (solid black line with stars) and IASI (solid black line with x signs) sensors, and simulated by the PM (dashed gray line with circles) and CPM (dashed gray line with squares) models between 16 June and 29 June 2018. (b) and (c) represent the sub-daily evolution of the 2-meter temperatures respectively over Matam and Podor with PM (dashed grey line), CPM (dashed black line), and observations (solid black line).

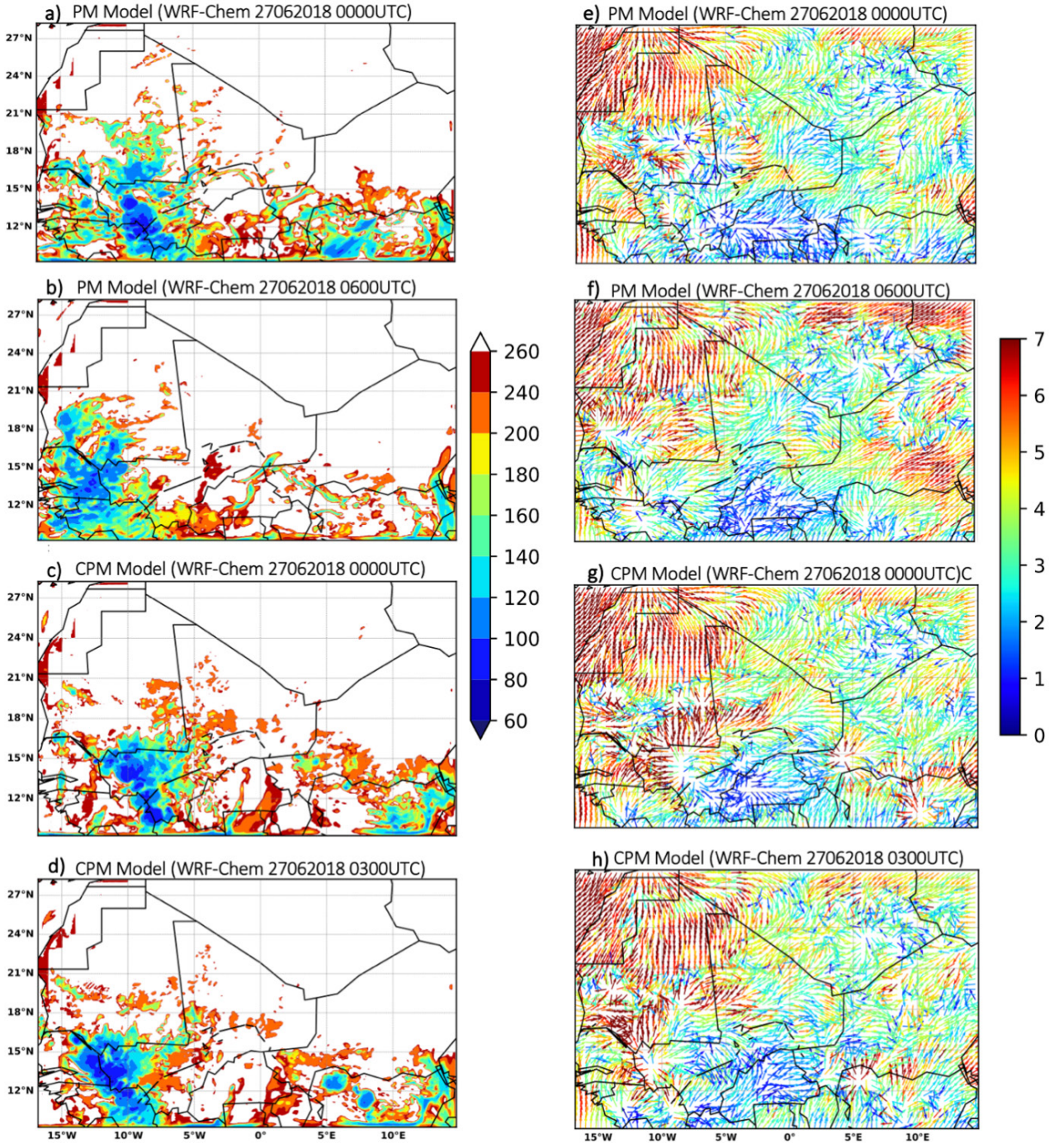

Figure 6. Outgoing Longwave Radiation (OLR) in $W \cdot m^{-2}$ respectively simulated by the PM at (a) 27 June 0000 UTC, (b) 27 June 0600 UTC, and CPM at (c) 27 June 0000 UTC and (d) 27 June 0300 UTC. 10-meter wind directions (arrow), and wind magnitudes (color shading) respectively simulated by PM at (a) 27 June 0000 UTC, (b) 27 June 0600 UTC, and CPM at (c) 27 June 0000 UTC and (d) 27 June 0300 UTC.

3.3 Environmental properties of the MCS

Figure 5c shows that both simulations reproduce the diurnal cycle of the surface temperature over the eastern side and northern side of Senegal with a better agreement with observation over Podor. Based on the surface temperature, simulations show an abrupt change related to the spreading of the MCS over West Africa on 26 and 27 June 2018 (**Figures 5b** and **4c** and **Figure 7**) as observed in synoptic scale (**Figures 4c** and **4d**). The minimum temperature shown by the observation at the detection time of the MCS over Matam is obtained in the simulations at 1200 UTC (**Figure 5**). **Figure 7i-7p** shows more details on the changes in 2-meter temperatures (T2m) induced by the MCS properties. By 2100 UTC on 26 June, significant dry air masses are located in the aerosol transect [48] over southern Algeria, northern Mali, southern Mauritania, and northeastern Senegal (**Figures 7i** and **7m**). By 0000 UTC on 27 June, a decrease of T2m of about 5 °C is noted on this transect when the MCS merged with northeastward convective cells (**Figures 7j** and **7n**). When the MCS is detected on the eastern side of Senegal and the western side of Mali (**Figures 6** and **7**), a significant gradient of temperature greater than 10 °C is obtained (**Figures 7k** and **7o**). By 1800 UTC on 27 June after the system spread away from West Africa, the situation becomes drier on the northern latitude 12°N (**Figures 7l** and **7p**).

The important transport of southwestward moisture, which is associated with oceanic air masses and powering the MCS on 27 June at 0000 UTC, is in **Figures 7b** and **7f** with precipitable water exceeding 50 mm. The cold pool is associated with 10-meter wind exceeding 20 $m \cdot s^{-1}$ and the migration of the ITD is located at northern Texte latitude 18°N during the event. The monsoon surge shown by the southwesterly wind direction at 925 hPa and the strong northward progression of the ITD transport humidity over the border of Mali-Algeria and Niger as already highlighted in a previous case study [22].

3.4 Vertical profile of storm environment

Figure 8 shows the differences in the thermodynamic structure preceding and associated with the spread of the cold pool. The atmosphere became increasingly moist, which is defined by the distance between the black and green lines, below 700 hPa when the MCS arrived at Matam with a maximum humidity located between 850 and 700 hPa in the PM model. The atmosphere is generally well mixed with the westward transport of air masses as shown in Figure 8 by wind directions above 800 hPa. The moisture transport is stronger in the PM than in CPM model (**Figure 8**), in contrast to the wind surface which shows respectively a magnitude contours of 11.5 $m \cdot s^{-1}$ and 24 $m \cdot s^{-1}$ (**Figure 7**). This result is in agreement with the founding [12], where authors showed that their Parameterized simulation has got a greater moisture convergence than their explicit model.

3.5 Impact of dust

In this section, we investigate the profile, T2m temperature, and daily precipitation between the Parameterized and explicit convection in WRF-Chem. On 27 June at 0000 UTC, the lowest atmosphere between the surface and 2 km is dryer in the explicit convection than in the model Parameterized (**Figures 8a** and **8c**). After the event on 27 June, the PM model showed heavy moisture between 850 hPa and 500 hPa (1.5 km to 3 km). The explicit convection is quick dryer at this altitude and above and is similar to the ERA5 vertical profile (not shown).

On 27 June, the observation from GPM-IMERG shows a spatial distribution of daily precipitation over the western Sahel, with a maximum over northern Burkina Faso, southern Mali, eastern Senegal, western African coastal, northern Nigeria and southwestern Niger (**Figure 9a**). The Parameterized and NODUST explicit convection models miss capture in general the maximum rain over West Africa expected in southeastern Senegal and overestimate the daily

precipitation in Central Senegal (**Figures 9b** and **9d**). However, the explicit convection captures well the spatial patterns of daily precipitation as shown by the observations except in central Mali, and southwestern Niger (**Figures 9c**). **Figure 10** shows the spatial patterns of T2m temperature between dust and no-dust explicit models. This shows that airborne dust clearly affects solar radiation by inducing a cooler surface temperature before the event (from 26 June 2100 UTC to 27 June 0000 UTC). The atmosphere is heated after dust plume transport over the Sahel on 27 June 1800 UTC (**Figure 10d**).

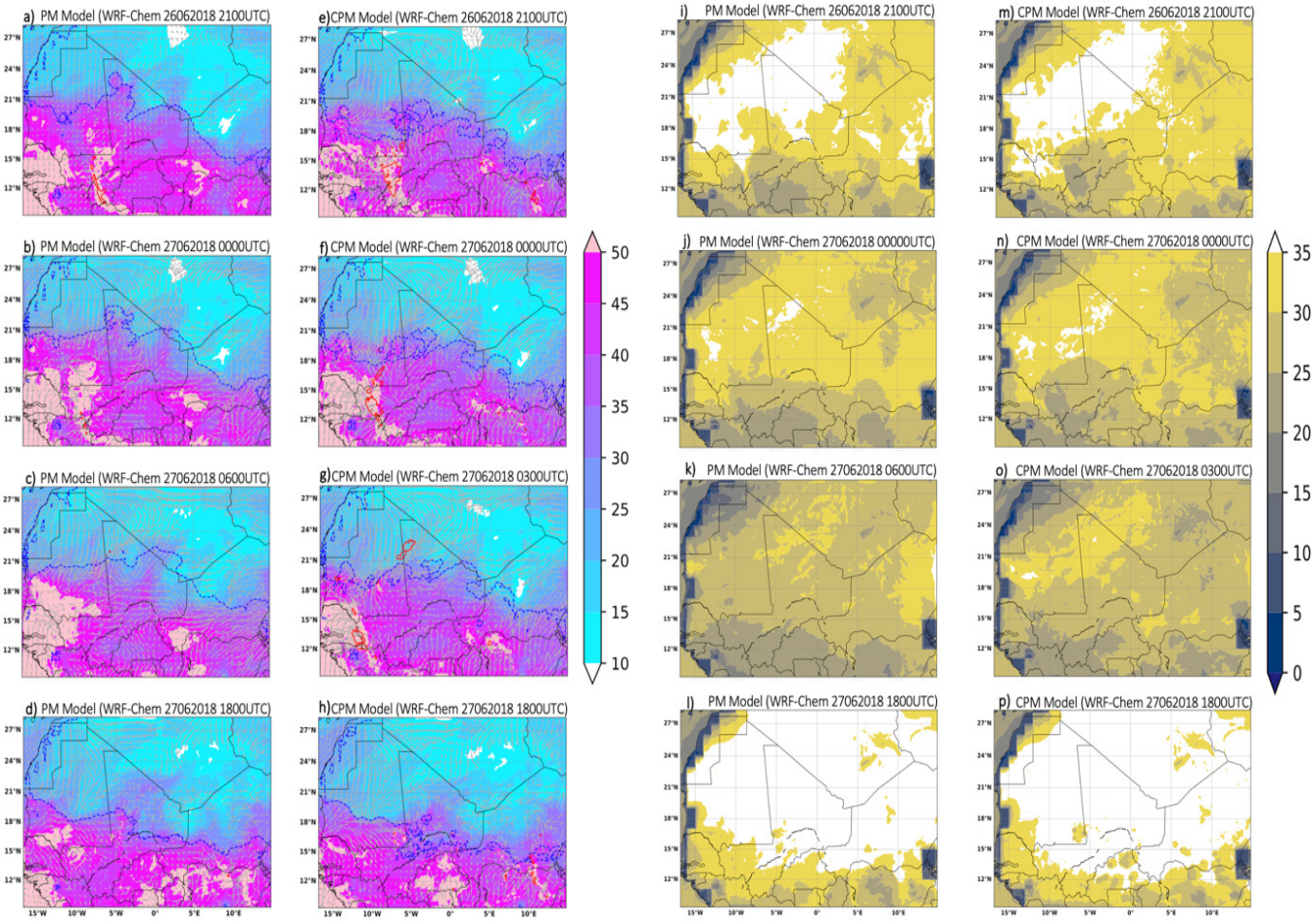

Figure 7. Precipitable Water Vapor (color shading) respectively simulated by the PM at (a) 26 June 2100 UTC, (b) 27 June 0000 UTC, (c) 27 June 0600 UTC, (d) 27 June 1800 UTC, and (e-h) by the CPM at the same time, and the ITD (dashed blue line) and 925 streamlines (grey). The 2 m surface temperature (color shading) respectively simulated by the PM (i-l), and the CPM (m-p) at the same time.

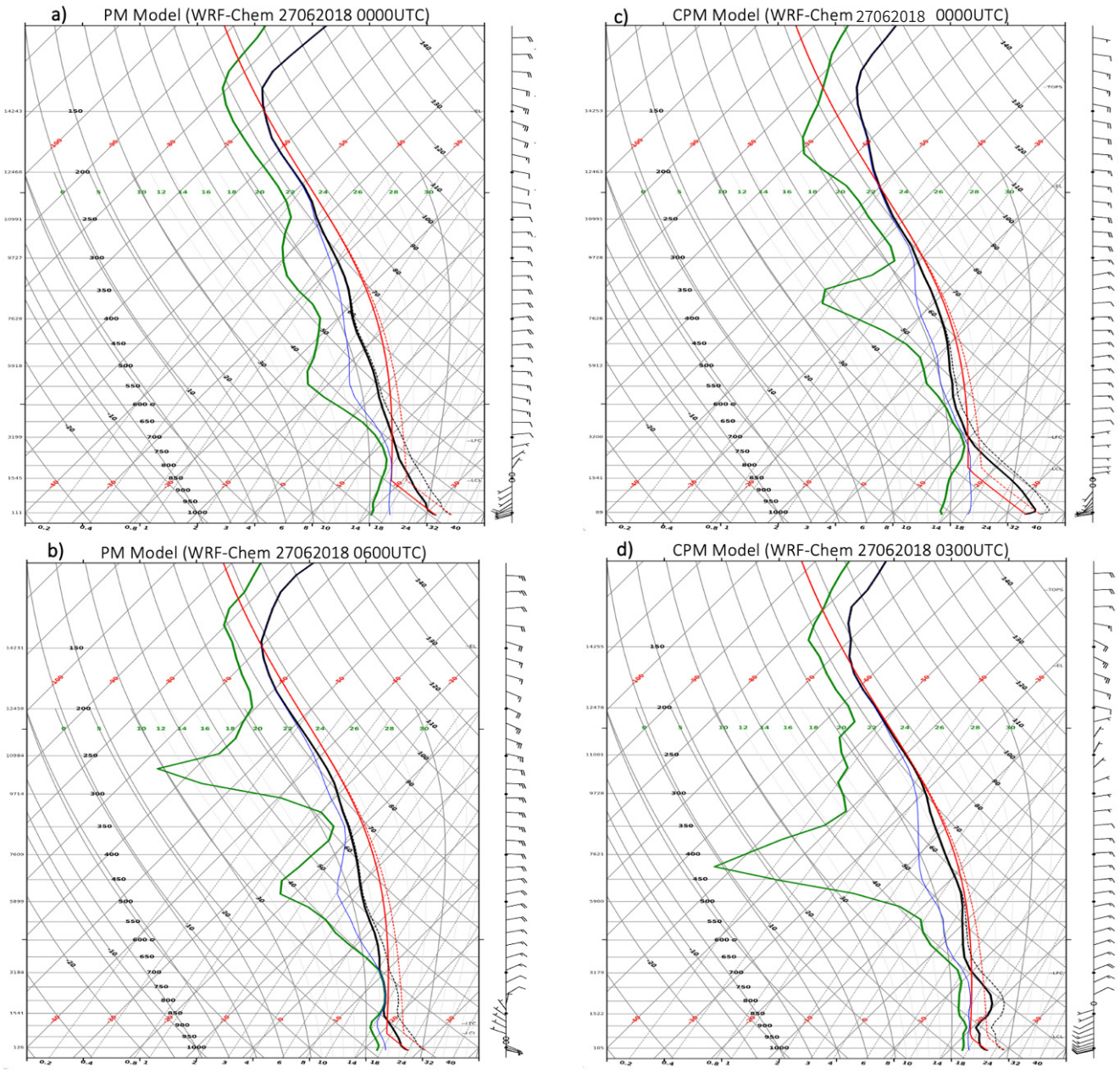

Figure 8. Skew-T diagram of simulated soundings over Matam (Senegal) respectively by the PM at (a) 27 June 0000 UTC, (b) 27 June 0600 UTC, and by the CPM at (c) 27 June 0000 UTC, and (d) 27 June 0300 UTC. Solid black and green show air and dew point temperatures (°C), and black wind barbs show the simulated winds in knots.

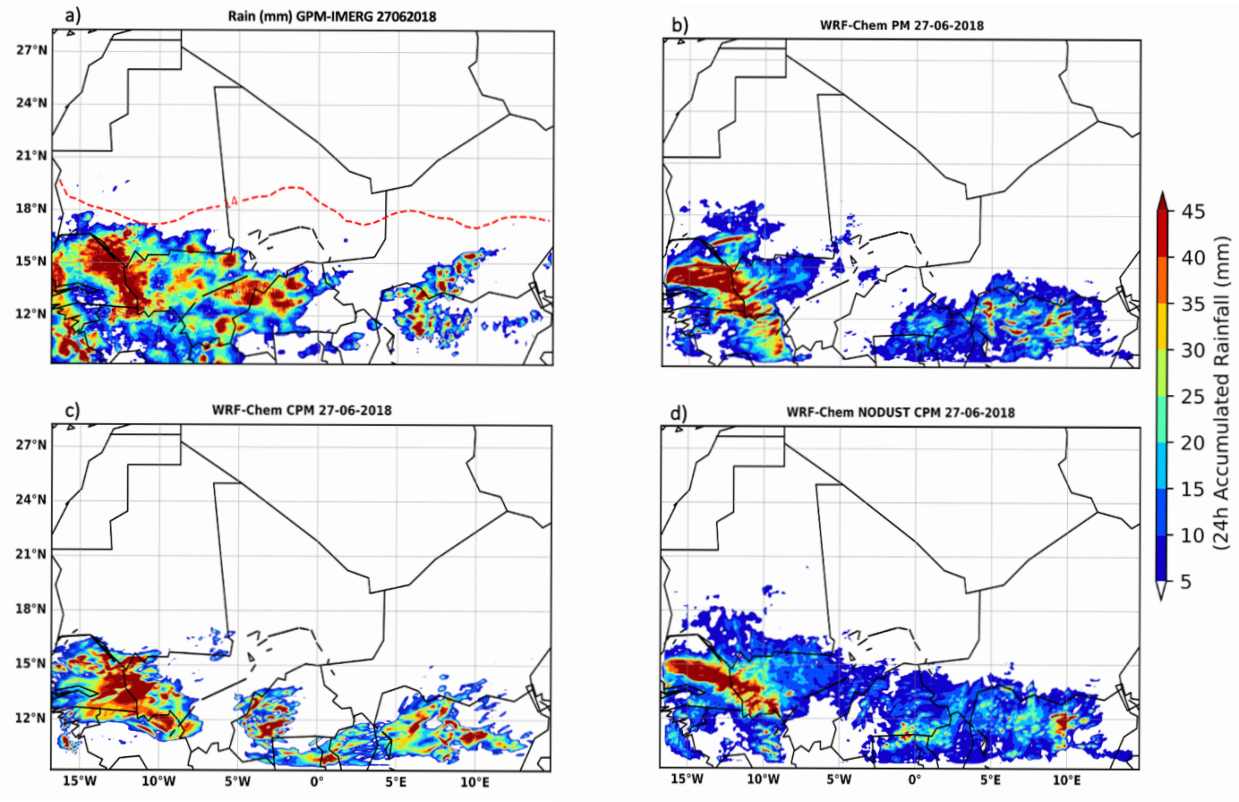

Figure 9. 24 h accumulated rainfall from GPM-IMERG (a), (b-d) accumulated modeled daily precipitation from respectively PM, CPM and NODUST models on 27 June.

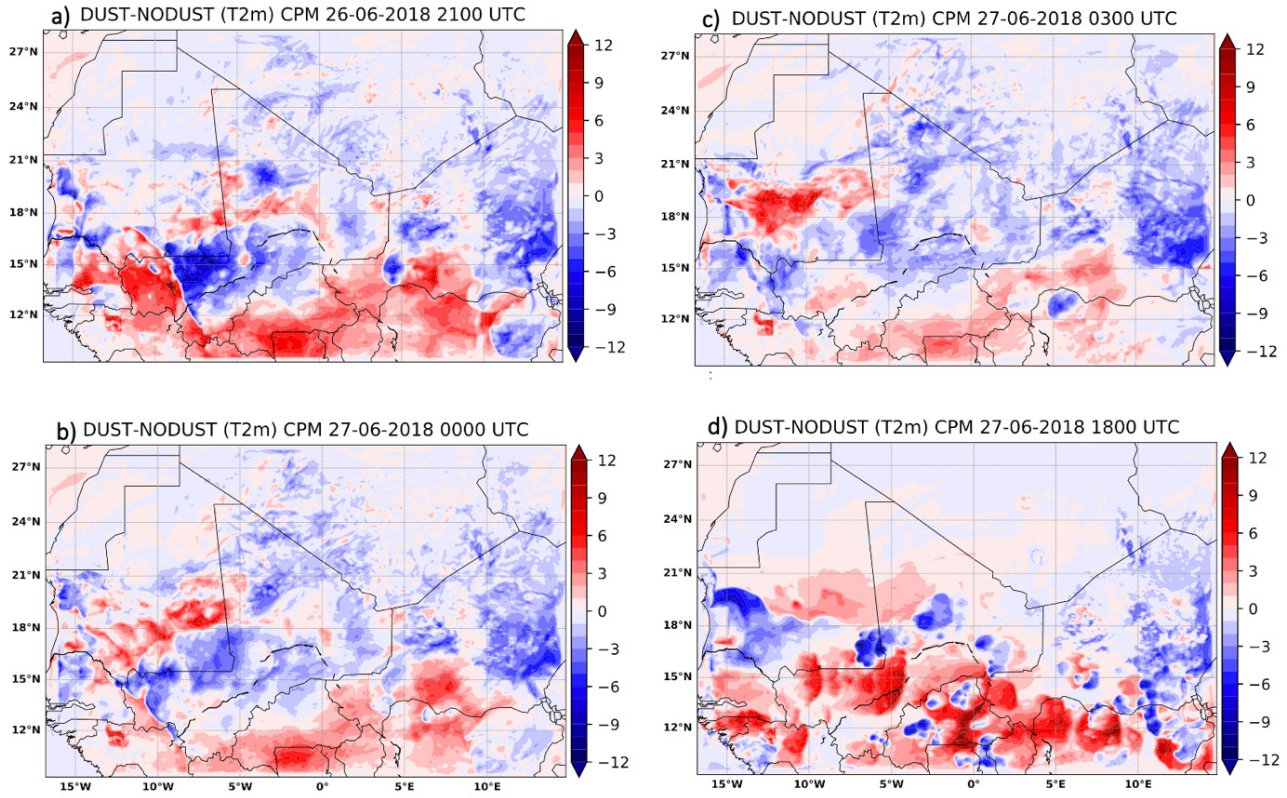

Figure 10. The difference in 2-meter temperatures (color shading) between Dust and NODUST CPM simulations at (a) 26 June 2100 UTC, (b) 27 June 0000 UTC, (c) 27 June 0300 UTC, and (d) 27 June 1800 UTC.

4. Conclusions

In this study, we have investigated the capability of WRF-chem model to capture a dust storm and the synoptic weather conditions that triggered a severe dust storm in West Africa between 26 and 27 June 2018 accompanied by the first precipitation in the early monsoon season. Observational data from synoptic stations and satellite estimations showed a typical characterization of a haboob event accompanied by a huge amount of dust mobilization along the LECCP. The West African weather is clearly improved in the CPM model with a better spatial pattern of the daily precipitation similar to the distribution shown by the satellite observations. The explicit convection model captures well the dust-generating winds, which are enough underestimated in the Parameterized convection model. The strong 10-meter winds have exceeded 20 m/s in the CPM model and 15 m/s in the PM model. These strong winds have induced heavy dust emission along the Sahelian dust transect and then impacted strongly the 2-m surface temperatures in both models. However, surface turbulence is better represented in the CPM than in the PM models. The heavy dust emitted in the CPM model has induced a strong gradient in the surface temperature with warmer and cooler air masses respectively onward and behind the MCS. The thermodynamic features showed that the characterization of haboob is matched in both simulations when the MCS spreading from North Burkina merges with small convective cells advected from central Mali on the night of 27 June 2018 as well as showed in the observations. The merging of the convective cells was coinciding with a strong southwest transport of air masses bringing moisture and then empowering the MCS.

Conflict of Interest

There is no conflict of interest.

Acknowledgment

The authors wish to thank the Global Challenges Research Fund (GCRF) African Science for Weather Information and Techniques (SWIFT) Programme. Thanks to NASA, CNES, ICARE and AERONET for providing access to CALIOP data and Sun photometer. We are grateful to the University Corporation for Atmospheric Research (UCAR) in Boulder, Colorado, for access to Cheyenne supercomputer.

References

[1] Levin, Z., Ganor, E., Gladstein, V., 1996. The effects of desert particles coated with sulfate on rain formation in the eastern Mediterranean. Journal of Applied Meteorology and Climatology. 35(9), 1511-1523.

[2] Wurzler, S., Reisin, T.G., Levin, Z., 2000. Modification of mineral dust particles by cloud processing and subsequent effects on drop size distributions. Journal of Geophysical Research: Atmospheres. 105(D4), 4501-4512.

[3] Rosenfeld, D., Rudich, Y., Lahav, R., 2001. Desert dust suppressing precipitation : A possible desertification feedback loop. Proceedings of the National Academy of Sciences. 98(11), 5975-5980.

[4] Martínez, I.R., Chaboureau, J.P., 2018. Precipitation and mesoscale convective systems : Radiative impact of dust over northern Africa. Monthly Weather Review. 146(9), 3011-3029.

[5] Camara, M., Jenkins, G., Konare, A., 2010. Impacts of dust on West African climate during 2005 and 2006. Atmospheric Chemistry and Physics Discussions. 10(2), 3053-3086.

[6] Kocha, C., Lafore, J., Tulet, P., et al., 2012. High-resolution simulation of a major West African dust-storm : Comparison with observations and investigation of dust impact. Quarterly Journal of the Royal Meteorological Society. 138(663), 455-470.

[7] Chaboureau, J., Tulet, P., Mari, C., 2007. Diurnal cycle of dust and cirrus over West Africa as seen from Meteosat Second Generation satellite and a regional forecast model. Geophysical Research Letters. 34(2).

[8] Janiga, M.A., Thorncroft, C.D., 2014. Convec-

tion over tropical Africa and the east Atlantic during the West African monsoon : Regional and diurnal variability. Journal of Climate. 27(11), 4159-4188.

[9] Mathon, V., Laurent, H., Lebel, T., 2002. Mesoscale convective system rainfall in the Sahel. Journal of Applied Meteorology. 41(11), 1081-1092.

[10] Roberts, A., Knippertz, P., 2014. The formation of a large summertime Saharan dust plume : Convective and synoptic-scale analysis. Journal of Geophysical Research: Atmospheres. 119(4), 1766-1785.

[11] Lin, Y.L., 2007. Mesoscale convective systems. Mesoscale dynamics. Cambridge University Press: Cambridge. pp. 322-378.
DOI: https://doi.org/10.1017/CBO9780511619649.010

[12] Finney, D.L., Marsham, J.H., Rowell, D.P., et al., 2020. Effects of explicit convection on future projections of mesoscale circulations, rainfall, and rainfall extremes over Eastern Africa. Journal of Climate. 33(7), 2701-2718.

[13] Birch, C., Parker, D., Marsham, J., et al., 2014. A seamless assessment of the role of convection in the water cycle of the West African monsoon. Journal of Geophysical Research: Atmospheres. 119(6), 2890-2912.

[14] Marsham, J.H., Dixon, N.S., Garcia-Carreras, L., et al., 2013. The role of moist convection in the West African monsoon system : Insights from continental-scale convection-permitting simulations. Geophysical Research Letters. 40(9), 1843-1849.

[15] Marsham, J.H., Knippertz, P., Dixon, N.S., et al., 2011. The importance of the representation of deep convection for modeled dust-generating winds over West Africa during summer. Geophysical Research Letters. 38(16).

[16] Pope, R., Marsham, J., Knippertz, P., et al., 2016. Identifying errors in dust models from data assimilation. Geophysical Research Letters. 43(17), 9270-9279.

[17] Hohenegger, C., Schlemmer, L., Silvers, L., 2015. Coupling of convection and circulation at various resolutions. Tellus A: Dynamic Meteorology and Oceanography. 67(1), 26678.

[18] Prein, A.F., Langhans, W., Fosser, G., et al., 2015. A review on regional convection-permitting climate modeling : Demonstrations, prospects, and challenges. Reviews of Geophysics. 53(2), 323-361.

[19] Crook, J., Klein, C., Folwell, S., et al., 2019. Assessment of the representation of West African storm lifecycles in convection-permitting simulations. Earth and Space Science. 6(5), 818-835.

[20] Stratton, R.A., Senior, C.A., Vosper, S.B., et al., 2018. A pan-African convection-permitting regional climate simulation with the Met Office Unified Model : CP4-Africa. Journal of Climate. 31(9), 3485-3508.

[21] Jackson, L.S., Keane, R.J., Finney, D.L., et al., 2019. Regional differences in the response of rainfall to convectively coupled Kelvin waves over tropical Africa. Journal of Climate. 32(23), 8143-8165.

[22] Trzeciak, T.M., Garcia-Carreras, L., Marsham, J.H., 2017. Cross-Saharan transport of water vapor via recycled cold pool outflows from moist convection. Geophysical Research Letters. 44(3), 1554-1563.

[23] Brindley, H., Knippertz, P., Ryder, C., et al., 2012. A critical evaluation of the ability of SEVIRI thermal IR RGB rendering to identify dust events. Part A: Theoretical analysis. Geophysical Research Letters. 117, D07201.

[24] Sayer, A., Munchak, L., Hsu, N., et al., 2014. MODIS Collection 6 aerosol products : Comparison between Aqua's e-Deep Blue, Dark Target, and "merged" data sets, and usage recommendations. Journal of Geophysical Research: Atmospheres. 119(24), 13-965.

[25] Clarisse, L., Coheur, P.F., Prata, F., et al., 2013. A unified approach to infrared aerosol remote sensing and type specification. Atmospheric Chemistry and Physics. 13(4), 2195-2221.

[26] Hsu, N., Jeong, M., Bettenhausen, C., et al., 2013. Enhanced Deep Blue aerosol retrieval algorithm : The second generation. Journal of

Geophysical Research: Atmospheres. 118(16), 9296-9315.

[27] Sayer, A., Hsu, N., Lee, J., et al., 2018. Satellite Ocean Aerosol Retrieval (SOAR) algorithm extension to S-NPP VIIRS as part of the "Deep Blue" aerosol project. Journal of Geophysical Research: Atmospheres. 123(1), 380-400.

[28] Wei, G., Lü, H., Crow, W.T., et al., 2018. Comprehensive evaluation of GPM-IMERG, CMORPH, and TMPA precipitation products with gauged rainfall over mainland China. Advances in Meteorology. 3024190.

[29] Hersbach, H., Bell, B., Berrisford, P., et al., 2020. The ERA5 global reanalysis. Quarterly Journal of the Royal Meteorological Society. 146(730), 1999-2049.

[30] Grell, G.A., Peckham, S.E., Schmitz, R., et al., 2005. Fully coupled "online" chemistry within the WRF model. Atmospheric Environment. 39(37), 6957-6975.

[31] Ginoux, P., Chin, M., Tegen, I., et al., 2001. Sources and distributions of dust aerosols simulated with the GOCART model. Journal of Geophysical Research: Atmospheres. 106(D17), 20255-20273.

[32] Hong, S.Y., Noh, Y., Dudhia, J., 2006. A new vertical diffusion package with an explicit treatment of entrainment processes. Monthly Weather Review. 134(9), 2318-2341.

[33] Chen, F., Dudhia, J., 2001. Coupling an advanced land surface-hydrology model with the Penn State—NCAR MM5 modeling system. Part I: Model implementation and sensitivity. Monthly Weather Review. 129(4), 569-585.

[34] Jiménez, P.A., Dudhia, J., González-Rouco, J.F., et al., 2012. A revised scheme for the WRF surface layer formulation. Monthly Weather Review. 140(3), 898-918.

[35] Iacono, M.J., Delamere, J.S., Mlawer, E.J., et al., 2008. Radiative forcing by long-lived greenhouse gases : Calculations with the AER radiative transfer models. Journal of Geophysical Research: Atmospheres. 113(D13).

[36] Mlawer, E.J., Taubman, S.J., Brown, P.D., et al., 1997. Radiative transfer for inhomogeneous atmospheres : RRTM, a validated correlated-k model for the longwave. Journal of Geophysical Research: Atmospheres. 102(D14), 16663-16682.

[37] Grell, G.A., Dévényi, D., 2002. A generalized approach to parameterizing convection combining ensemble and data assimilation techniques. Geophysical Research Letters. 29(14), 381-384.

[38] Hong, S.Y., Dudhia, J., Chen, S.H., 2004. A revised approach to ice microphysical processes for the bulk parameterization of clouds and precipitation. Monthly Weather Review. 132(1), 103-120.

[39] Jenkins, G.S., Gueye, M., 2018. WRF 1960-2014 winter season simulations of particulate matter in the Sahel : Implications for air quality and respiratory health. GeoHealth. 2(8), 248-260.

[40] Khan, B., Stenchikov, G., Weinzierl, B., et al., 2015. Dust plume formation in the free troposphere and aerosol size distribution during the Saharan mineral dust experiment in North Africa. Tellus B: Chemical and Physical Meteorology. 67(1), 27170.

[41] Ukhov, A., Mostamandi, S., da Silva, A., et al., 2020. Assessment of natural and anthropogenic aerosol air pollution in the Middle East using MERRA-2, CAMS data assimilation products, and high-resolution WRF-Chem model simulations. Atmospheric Chemistry and Physics. 20(15), 9281-9310.

[42] Senghor, H., Roberts, A.J., Dieng, A.L., et al., 2021. Transport and deposition of Saharan dust observed from satellite images and ground measurements. Journal of Atmospheric Science Research. 4(2), 1-11.

[43] Allen, C.J., Washington, R., Engelstaedter, S., 2013. Dust emission and transport mechanisms in the central Sahara : Fennec ground-based observations from Bordj Badji Mokhtar, June 2011. Journal of Geophysical Research: Atmospheres. 118(12), 6212-6232.

[44] Washington, R., Bouet, C., Cautenet, G., et al.,

2009. Dust as a tipping element : The Bodélé Depression, Chad. Proceedings of the National Academy of Sciences. 106(49), 20564-20571.

[45] Alonso-Pérez, S., Cuevas, E., Querol, X., et al., 2012. African dust source regions for observed dust outbreaks over the subtropical Eastern North Atlantic region, above 25 N. Journal of Arid Environments. 78, 100-109.

[46] Westphal, D.L., Toon, O.B., Carlson, T.N., 1987. A two-dimensional numerical investigation of the dynamics and microphysics of Saharan dust storms. Journal of Geophysical Research: Atmospheres. 92(D3), 3027-3049.

[47] Kousky, V.E., 1988. Pentad outgoing longwave radiation climatology for the South American sector. Revista Brasileira de Meteorologia. 3(1), 217-231.

[48] Mortier, A., Goloub, P., Derimian, Y., et al., 2016. Climatology of aerosol properties and clear-sky shortwave radiative effects using Lidar and Sun photometer observations in the Dakar site. Journal of Geophysical Research: Atmospheres. 121(11), 6489-6510.